Title
Orbital forcing of the East Antarctic ice sheet during the Pliocene and Early Pleistocene

Journal
Nature Geoscience, 7(11)

ISSN
1752-0894

Authors
Patterson, MO
McKay, R
Naish, T
et al.

Publication Date
2014-11-05

DOI
10.1038/ngeo2273

Peer reviewed

Response of the East Antarctic Ice Sheet to orbital forcing during the Pliocene and early Pleistocene

Patterson, M. O.[1]*, McKay, R.[1], Naish, T.[1], Escutia, C.[2], Jimenez-Espejo, F. J.[3, 4], Raymo, M[5]., Tauxe, L.[6], Brinkhuis, H.[7], and IODP Expedition 318 Scientists

1) Antarctic Research Centre, Victoria University of Wellington, Wellington, New Zealand
2) Instituto Andaluz de Ciencias de la Tierra, CSK – University of Granada, Granada, Spain
3) Department of Earth and Planetary Sciences, Graduate School of Environmental Studies, Nagoya University, Nagoya, Japan.
4) Institute of Biogeosciences, Japan Agency for Marine-Earth Science and Technology, Yokosuka, Japan.
5) Lamont-Doherty Earth Observatory of Columbia University P.O. Box 1000, 61 Route 9W, Palisades, NY, 10964
6) Scripps Institution of Oceanography, La Jolla, CA 92093-0220, USA
7) Marine Palynology and Paleoceanography, Laboratory of Paleobotany and Palynology, Utrecht University, Budapestlaan 4, 3584 CD Utrecht, NL

*Corresponding author: molly.patterson@vuw.ac.nz

Geological reconstructions of global ice volume[1] and sea-level[2] during the Pliocene and Early Pleistocene (5 to 2 Ma) display regular glacial-interglacial cycles occurring every 41-kyrs, paced by variations in Earth's axial tilt (obliquity). The absence of a strong ~20-kyr precession signal challenges our fundamental understanding of how ice sheets

respond to orbital forcing because precession should impart the greatest influence on high-latitude summer insolation intensity, and therefore polar ice volume[3,4]. While a number of hypotheses have been proposed[4,5,6], reconciliation of this conundrum remains hampered by a lack of observational evidence from the Antarctic ice sheet. Here, we present an orbital-scale time-series of ice-berg rafted debris and continental rise sedimentation from a well-dated sediment core (Integrated Ocean Drilling Program site U1361) adjacent to the Wilkes Land margin of the East Antarctic Ice Sheet (EAIS). Our data reveal ~40-kyr cyclic variations in the extent of the EAIS paced by obliquity between 4.3-3.3 Ma during the warmer-than-present climate of the Pliocene, as has previously been demonstrated for the West Antarctic Ice Sheet (WAIS)[7,8]. Under a warmer climate state, mean annual insolation (paced by obliquity) had more influence on Antarctic ice volume, than insolation intensity modulated by precession[6]. However, a transition to 20-kyr precession cycle dominance at 3.3 Ma preceded the development of a more stable EAIS marine margin at ~ 2.5 Ma, reflecting the declining influence of oceanic forcing as the high latitude southern ocean cooled and a perennial summer sea-ice field developed[9]. Our data shows that precession-paced EAIS variability occurs during cold climate states, even when the obliquity signal dominates globally-integrated proxy records, lending support to the hypothesis that anti-phased polar ice-volume cancels out on a precession time scale[4].

A new marine sediment core (U1361) recovered by the Integrated Ocean Drilling Program (IODP) from ~3000 m water depth on the continental rise adjacent to the Wilkes Land sector of Antarctica (Fig. 1; Extended Data Fig. 1) provides a well-dated and continuous geological archive of Pliocene and Early Pleistocene orbital scale variability of the marine margin of the EAIS. Sediment deposition at this site is controlled by the interplay between: (i) downslope marine sediment gravity flows triggered by the buildup of sediment on the edge of the continental shelf during glacial advance; (ii) the rainout of biogenic detritus from surface water plankton; (iii) iceberg rafting of terrigenous sediments and (iv) low energy bottom currents (Supplementary Information).

The core consists of eighteen sedimentary cycles spanning an age range of 4.3-2.2 Ma, and comprising alternating terrigenous massive to laminated muds and diatom-rich/bearing silty muds units (cycles 1-18 Fig. 2; Extended Data Fig. 2, 3). In places the muds contain packages of well-defined laminae and are consistent with established models of non-erosive overbank hemipelagic deposition onto a channel levee setting via turbidites on the lowermost Antarctic continental rise[10]. Steeply dipping, seaward prograding wedge sediments are evident in seismic reflection profiles across the continental shelf and extend onto the upper continental slope above seismic unconformity WL-U8 (~4.2 Ma)[11,12] (Extended Data Fig. 1). The geometry of these strata is characteristic of grounding zone deposition by repetitive advances of a marine based ice sheet to the shelf edge during glacial periods[12]. Sediment overloading near the shelf break at submarine canyons heads, in turn triggers turbidity currents down slope channels and leads to overbank deposition at the core site. Low density turbidity currents in overbank “distal” channel level environments on Antarctic continental rise are typically non erosiove[10] (Supplementary Information). Thus, turbidite units are associated with periods of glacial advance to the Wilkes Land continental shelf edge, whereas bioturbated, diatom-rich/bearing facies represent warm interglacial periods of relatively ice-free ocean and increased primary productivity when the grounding line had migrated landward away from the shelf edge. Increased productivity during interglacial warm climates may be associated with enhanced upwelling of nutrient-rich Circumpolar Deepwater (CDW)[13] (Supplementary Information), which has been linked to southward expansion of the westerly wind field in response to a reduced pole-equator temperature gradient during past warm periods[14]. Presently this relatively warm nutrient-rich CDW upwells to the surface north of the Southern Boundary Front of the Antarctic Circumpolar Current and is marked by areas of enhanced productivity immediately to the north of Site U1361 (Fig. 1).

We have developed a high-resolution record (~3-4 kyr sample spacing) of ice-berg rafted debris (IBRD) mass accumulation rates (MAR) and opal deposition for the U1361 core (Methods; Extended Data Table 1; Extended Data Fig. 4). Our age model is based on biostratigraphy used to constrain the interpretation of a magnetic polarity stratigraphy[11], and for our initial spectral analysis we have assumed constant, long-term (millennial-scale) sedimentation rates between polarity reversal tie points (Methods; Extended Data Fig. 5).

In general the highest intensity of IBRD occurs during transitions from glacial terrigenous mud facies to interglacial diatom-rich/bearing muds up-core until ~47 mbsf, with most IBRD peaks immediately preceding opal peaks (Fig. 2). Isotopic Nd and Sr provenance indicators suggest that the terrigenous components in these diatom-rich/bearing muds are associated with periods of deglacial retreat of the ice margin back into the Wilkes Land subglacial basin during the Early Pliocene[15]. As the Antarctic ice sheet loses the majority of its mass via icebergs[16], we interpret the maxima in IBRD MAR to be the consequence of accelerated calving during glacial retreat from marine terminating outlet glaciers along the Wilkes Land coastline as well as a contribution from EAIS outlet glaciers entering the western Ross Sea (Methods; Supplementary Information). This interpretation is consistent with models and paleo-observations, which imply the most rapid mass loss of the EAIS margin during the last glacial termination occurred between 12-7 ka, and was primarily the consequence of oceanic warming[17].

Spectral analysis of the un-turned IBRD MAR time-series displays a dominant period of ~40-kyr between ~4.3-~3.4 Ma, which transitions to strong variance at ~20-kyr periods after ~3.3Ma, with a corresponding decrease in power of the ~40-kyr cycle between 3.3-2.2 Ma (Fig. 2h, 2i; Extended Data Fig. 6). On the basis of this strong orbital relationship displayed in frequency spectra of the untuned IBRD MAR time series (Fig. 2), an independent age model, and near continuous and uniform long-term sedimentation (Extended Data Fig. 5), we establish a graphical one-to-one correlation between cycles in ice margin variability expressed by our IBRD data and orbitally-paced climatic time series. Between 4.3-3.3 Ma there is a very strong correlation between 41-kyr cycles mean annual insolation and the benthic $\delta^{18}O$ global ice volume record[1], whereas, between 3.3-2.2 Ma IBRD cycles correlate with the ~20-kyr cycles of summer insolation at 65°S (Fig. 2). We acknowledge that although our visual correlations are constrained by 7 precisely-dated paleomagnetic reversals, they may not represent a unique solution, but as noted above they are entirely consistent with the variance in orbital frequencies implied by our spectral estimations. We then used the graphical relationships in Fig. 2 to explore the role of longer-period orbital influences on the pattern of iceberg calving (Online Methods; Supplementary Information). The top of the ~40-kyr-dominated interval is marked by a ~300-kyr-long condensed section between ~3.6-3.3 Ma (Fig. 2; Extended Data Fig. 5), and corresponds to a +1‰ glacial $\delta^{18}O$ excursion spanning Marine Isotope Stage (MIS) MG9 and MIS M2. Indeed, this glacial excursion has also been associated with southern high-latitude climate cooling and the re-establishment of grounded ice on middle to outer continental shelf in the Ross Sea following a ~200-kyr period of warm open ocean conditions[7,9]. Previous studies of older Oligocene and Miocene $\delta^{18}O$ glacial excursions have proposed a relationship between intervals of increased glacial amplitude in the $\delta^{18}O$ record with a coincidence of 1.2 Ma nodes in obliquity and 400-kyr minima in long period eccentricity[18,19]. This orbital configuration, which favours extended periods of cold summers and low seasonality is considered optimal for Antarctic ice sheet expansion, and occurs at ~3.3 Ma - the time of the transition from ~40-yr to ~20-kyr dominance in the IBRD MAR times series from U1361 (Fig. 2).

We developed orbital-tuning strategy based on the strong orbital signal in our un-tuned IBRD MAR record, and the clear link between peaks and troughs in austral summer insolation, IBRD MAR and opal content which are synchronous across that top and bottom Kaena Subchron paleomagnetic reversals, respectively (Fig. 3a, and discussed below). Band-pass filters at obliquity and precession frequencies applied to the IBRD MAR confirm visual observations that long-term minima are associated with (eccentricity-modulated) nodes in precession after 3.3 Ma, and the obliquity node at 4.1 Ma (Fig 3b; Extended Data Fig. 7).

Observed ~20-kyr-duration IBRD cycles correlated with summer insolation calculated for 65°S for the interval of the core between 3.3-2.2 Ma (Fig. 2; Fig. 3a), are embedded within 100-kyr-duration IBRD cycles (Fig. 2i), with broad peaks of IBRD maxima associated with transitions between laminated mudstones to diatom-rich/bearing muds (Fig. 2b). Although this lithological variability is also evident in frequency spectra of opal percentage, it is not significant at 90% (Extended Data Fig. 6, 7), which is the likely consequence of a lower signal-to-noise ratio in the opal data (Methods; Extended Data Fig. 8). A dramatic decrease in the amplitude of ~20-kyr IBRD peaks, and a change to lithofacies associated with non-erosive low-energy bottom currents at the core site from ~2.5 Ma is broadly coincident with southern high latitude cooling[9] and the onset of major Northern Hemisphere glaciations[9,20]. We attribute the progressive reduction in calving intensity to cooling and a relative stabilization of the EAIS ice margin. Homogenization of the turbidite sediments during glacial maxima by enhanced bioturbation and bottom current activity is observed and likely reflects increased Antarctic sea ice and polynya-style mixing at this time producing oxygenated high salinity shelf water[9], transferred downslope over Site U1361 to form Antarctic Bottom Water[21] (Supplementary Information).

In summary, our correlations of variations in IBRD and opal content with the benthic $\delta^{18}O$ stack and orbital time series (Fig. 2) identify up to sixteen ~40-kyr-duration cycles within six major lithological cycles (cycles 13-18 Fig. 2) during the early Pliocene (4.3-3.3 Ma). This is followed by forty-two ~20-kyr-duration cycles, within twelve longer-duration lithological cycles (cycles 1-12 Fig. 2).

Although, the marine sediment core recovered by the ANDRILL Program from the Ross Sea region provided the first direct evidence, that advance and retreat of the WAIS margin across the continental shelf was paced by obliquity during the Pliocene prior to ~3 Ma[7], sub-glacial erosion surfaces in the ANDRILL core associated with ice advance have raised the possibility of missing cycles, particularly after 3.1 Ma. The continuous U1361 record presented here confirms the dynamic in phase response, not only of the WAIS but also the marine margins of the EAIS, to obliquity forcing during the warm Pliocene prior to the onset of southern high-latitude cooling at 3.3 Ma.

Geological records[7,9,15] and model simulations[8] of recent and past warm climates both highlight the sensitivity of the marine-based portions of the Antarctic ice sheets to ocean warming, but the mechanism by which the coastal ocean warms and destabilises marine grounding lines in response to obliquity forcing remains elusive. It has been proposed that changes in the intensity and the meridional distribution of mean annual insolation controlled by obliquity may have a profound influence on the position and strength of the Southern Hemisphere zonal westerly winds[7]. Indeed, an aerosolic dust record from the Southern Ocean is dominated by ~40-kyr cycles in iron and leaf-wax biomarkers of prior to ~0.8 Ma[22]. Moreover, prior to ~3.3 Ma the southward expansion of the westerly wind-field over the Antarctic circumpolar convergence zone under a reduced meridional temperature gradient has been associated with a reduced sea-ice field[9], and the upwelling of warm, CO_2-rich Circumpolar Deep Water (CDW)[14,23] onto the continental shelf with consequences for the stability of marine grounding-lines[24]. The dominance of precession-paced variability and the corresponding reduction in obliquity influence revealed by our data after ~3.3 Ma is interpreted to reflect a declining influence of oceanic forcing on EAIS stability and extent, as the southern high latitudes cooled. Both model and geological reconstructions imply that past Antarctic ice sheet expansion is closely linked with development of the sea-ice field[25] potentially resulting in northward migration of westerly winds and Southern Ocean fronts[9]. In addition, sea ice expansion after 3.3 Ma likely restricted upwelling and ventilation of warm CO_2 rich CDW at the Antarctic margin acting to further enhance climate cooling, which has been linked in models to a change in the frequency of the orbital response of polar ice sheets[26]. Under such a scenario, a warmer climate state during the Early to mid-Pliocene with higher atmospheric CO_2 concentration[27] required less insolation to melt sea ice, thus extending the austral melt season with its duration more strongly influenced by mean annual insolation controlled by obliquity (Fig. 2d), rather than seasonal insolation intensity controlled by precession[6]. Late Pliocene cooling raised the melt threshold such that the duration of the melt season was restricted to times of austral summer insolation maxima controlled by precession (Fig. 2c), with extensive sea-ice cover for much of the summer season limiting the influence of CDW on marine grounding line instability. This supports the notion that the length of the summer melt season is controlled by the overall climate state, and is the primary influence on the frequency response of the EAIS to orbital forcing[7].

Our data also supports the general concept of precession-driven, antiphase oscillations in inter hemispheric ice volume that may be cancelled out in globally integrated proxy records between ~3.3-2.5 Ma (e.g. ref. 4). Furthermore, by using paleomagnetic reversals from the bottom and top of the Kaena Subchron, to synchronise proxy reconstructions of summer climate in Antarctica (U1361) and the Arctic (Lake El'gygytyn)[28], we demonstrate a clear anti-phased response to precessional forcing on inter hemispheric climate (Fig. 3a; Extended Data Table 2). However, the argument that the intensity of summer insolation was a direct control on surface melt of a dynamic EAIS with a terrestrial ablation margin is not supported by this study. The geometry of strata on the Wilkes Land continental shelf indicate that the EAIS periodically expanded towards the continental shelf edge during glacial maxima in the Pliocene[12] (Extended Data Fig. 1) and suggests most Antarctic ice volume variance at this time was growth and retreat of the marine-based ice sheets. Indeed, iceberg calving appears to be associated with sea-ice melt as evidenced by the covariance of IBRD peaks with facies transitions going from relatively colder glacial maxima conditions to warmer interglacial minima conditions as implied by open ocean primary productivity (opal) in our data. This is particularly true for the Late Pliocene from 3.3 to 2.5 Ma, but during the Early Pliocene, when the sea ice field was reduced and the ice sheet was in more direct contact with oceanic influences, iceberg calving occurred more regularly within both glacial and interglacial facies. Based on the significant decrease in IBRD after 2.5 Ma (Fig. 2; 3) and Southern Ocean records inferring decreased SSTs[9,29] , we also infer the EAIS started to stabilize and became less sensitive to ocean induced melting compared to the WAIS[24], with fully-glaciated East Antarctic ice volume fluctuating by a similar magnitude to that of Late Pleistocene glacial cycles (e.g. 15-20 m ice volume equivalent sea level)[8]. Notwithstanding this relative stability, ~20-kyr-duration Antarctic ice volume fluctuations of this magnitude could have offset a larger out-of-phase precessional change in Northern Hemisphere ice volume (e.g. 20-40m), resulting in an enhanced obliquity signal in globally integrated proxy records between 3.33 and 1.0 Ma[4]. Notwithstanding this, a range of proxy evidence including ice rafted debris records[20] and a recent dust flux record[30] confirm that NH ice sheet variability and climate primarily responded to obliquity. In contrast, our results imply that Southern Ocean sea-ice feedbacks caused a fundamentally different response of the marine-based sectors of the EAIS under a cooler Late Pliocene/Early Pleistocene climate state, characterized by a dominance of precession-paced variability.

We conclude that prior to the development of Northern Hemisphere ice sheets at ~3.3 Ma, East Antarctic Ice Sheet variability responded primarily to obliquity and demonstrated high sensitivity on orbital timescales to a relatively small increase in atmospheric CO_2 concentration and mean global surface temperature. With atmospheric CO_2 concentrations and global surface temperatures projected to remain above 400 ppm and >+2°C beyond 2100[31], our results suggest that the marine margins of EAIS ice sheet as well as the marine-based WAIS, will become increasingly susceptible to ocean-forced melting providing the potential for widespread mass loss raising sea-level by meters over the coming centuries.

Methodology

20cc samples were treated with H2O2 to remove organic material and 2M NaOH to remove biogenic opal for grain size analysis. The dry weights of the samples were measured before and after opal removal to obtain an opal weight and terrigenous weight percent. The covariance of the opal weights to the Ba/Al (a productivity indicator) from XRF scans of the core indicates that the majority of opal dissolved was due to diatom productivity rather than volcanic glass (Extended Data Figure 8). Opal percentages also correspond well to the independently determined visual core descriptions using smear slide estimates of biogenic opal content. Biogenic content was dissolved from the 250 µm to 2 mm fraction of coarse sand used to indicate IBRD. The MAR of the coarse sand fraction was then estimated using the following equation:

$$\text{IBRD MAR} = \text{CS\%} * \text{DBD} * \text{LSR}$$

where IBRD MAR is the mass accumulation rate (g/cm^2/k.y.), CS% is the terrigenous coarse-sand weight percent, DBD is the dry-bulk density of the nearest value (g/cm^3) and LSR is the interval average linear sedimentation rate (cm/k.y.). Visual examination of every individual sample for authigenic minerals and volcanic glass was conducted and these were absent, indicating that the IBRD volume percent was directly equivalent to the terrigenous CS%[32].

The distribution of mm-scale silt and sand laminae (with rare cm-scale beds) was collected using high-resolution line scan images of the split core face. The thickness and stratigraphic depth of each laminae was accurately mapped through the use of a purpose built image analysis script in Matlab©.

Using the age model of[11] we performed a basic spectrogram analysis script in Matlab© followed by power spectral analysis using the Multi-Taper method (MTM)[33] with five data tapers for the untuned IBRD MAR and biogenic opal time series at ~3 kyr resolution. Equal time spacing was achieved by linear interpolation. Time series for power spectra was broken into two segments as there is a gap in our data exceeding 100 kyrs that predates 3.33 Ma. The statistical significance of spectral peaks was tested relative to the null hypothesis of a robust red noise background, AR(1) modeling of median smoothing, at a confidence level of 90% and 95%[34].

Author Contributions

MOP, RM, TN designed the study, conducted sedimentological and time series analyses and wrote the paper. CE and HB led IODP Expedition 318 and provide seismic reflection data interpretation. FJ and CE analysed XRF geochemical data. LT led development of the age model. MR contributed to writing the manuscript. All authors contributed to the interpretations.

*Integrated Ocean Drilling Program Expedition 318 Scientists

Klaus, A[1], Fehr, A[2], Bendle, J. A. P.[3], Bijl, P. K.[4] , Bohaty., S.M.[5], Carr, S. A.[6], Dunbar, R. B.[7], Flores, J.A.[8], Gonzalez, J.J.[9], Hayden, T. G.[10], Iwai, M.[11], Katsuki, K.[12], Kong, G. S.[13], Nakai, M.[14], Olney, M. P.[15], Passchier, S.[16], Pekar, S. F.[17], Pross, J.[18], Riesselman, C.R.[19], Röhl, U.[20], Sakai, T.[21], Shrivastava, P. K.[22], Stickley, C. E.[23], Sugasaki, S.[24,25], Tuo, S.[26], van de Flierdt, T.,[27] Welsh, K.[28] , Williams, T.,[29] & Yamane, M.[30]

[1]United States Implementing Organization, Integrated Ocean Drilling Program, Texas A&M University, 1000 Discovery Drive, College Station, TX 77845, USA. [2]RWTH Aachen University, Institute for Applied Geophysics and Geothermal Energy, Mathieustrasse 6, D-52074 Aachen, Germany. [3]Geographical and Earth Sciences, University of Glasgow, Gregory Building, Lilybank Gardens, G128QQ Glasgow, UK. [4]Department of Chemistry and Geochemistry, Colorado School of Mines, 1500 Illinois Street, Golden, CO 80401, USA. [5]Ocean and Earth Science, National Oceanography Centre Southampton, University of Southampton, European Way, SO14 3ZH, Southampton, UK. [6]Department of Geological and Environmental Sciences, Stanford University, 325 Braun Hall, Building 320, Stanford, CA 94305-2115, USA. [7]Department of Environmental Earth System Science, Stanford University, 325 Braun Hall, Building 320, Stanford, CA 94305-2115, USA. [8]Department of Geology, Universidad de Salamanca, 37008, Salamanca, Spain. [9]Instituto Andaluz de Ciencias de la Tierra, CSIC-UGR, 18100 Armilla, Spain.[10]Department of Geology, Western Michigan University, 1187 Rood Hall, 1903West Michigan Avenue, Kalamazoo, MI 49008, USA. [11]Department of Natural Science, Kochi University, 2-5-1 Akebono-cho, Kochi 780-8520, Japan. [12]Geological Research Division, Korea Institute of Geoscience and Mineral Resources, 30 Gajeong-dong, Yuseong-gu, Daejeon 305-350, Republic of Korea. [13]Petroleum and Marine Research Division, Korea Institute of Geoscience and Mineral Resources, 30 Gajeong-dong, Yuseong-gu, Daejeon 305-350, Republic of Korea. [14]Education Department,

Daito Bunka University, 1-9-1 Takashima-daira, Itabashi-ku, Tokyo 175-8571, Japan. [15]Department of Geology, University of South Florida, Tampa, 4202 East Fowler Avenue, SCA 528, Tampa, FL 33620, USA. [16]Earth and Environmental Studies, Montclair State University, 252 Mallory Hall, 1 Normal Avenue, Montclair, New Jersey 07043, USA. [17]School of Earth and Environmental Sciences, Queens College, 65-30 Kissena Boulevard, Flushing, NY 11367, USA. [18]Paleoenvironmental Dynamics Group, Institute of Geosciences, Goethe-University Frankfurt, Altenhöferallee 1, 60438 Frankfurt, Germany. [19]Departments of Marine Science and Geology, University of Otago, PO Box 56, Dunedin 9054, New Zealand.[20]MARUM – Center for Marine Environmental Sciences, University of Bremen, Leobener Straße, 28359 Bremen, Germany. [21]Department of Geology, Utsunomiya University, 350 Mine-Machi, Utsunomiya 321-8505, Japan. [22]Antarctica Division, Geological Survey of India, NH5P, NIT, Faridabad 121001, Harlyana, India. [23]Department of Geology, Universitet i Tromsø, N-9037 Tromsø, Norway. [24]Scripps Institution of Oceanography, University of California, San Diego, La Jolla, California 92093-0220, USA, [25]Department of Earth and Planetary Sciences, University of Tokyo, 7-3-1 Hongo, Bunkyo-ku, Tokyo 113-0033, Japan. [26]School 223 of Ocean and Earth Science, Tongji University, 1239 Spring Road, Shanghai 200092, People's Republic of China. [27]Department of Earth Science and Engineering, Imperial College London, South Kensington Campus, Prince Consort Road, London SW7 2AZ, UK.[28]School of Earth Sciences, University of Queensland, St Lucia, Brisbane QLD 4072, Australia. [29]Lamont Doherty Earth Observatory of Columbia University, PO Box 1000, 61 Route 9W, Palisades, New York 10964, USA. [30]Earth and Planetary Science, University of Tokyo, 7-3-1 Hongo, Bunkyo-ku, Tokyo 113-0033, Japan.

REFERENCES

1. Lisiecki, L. E. & Raymo, M. E. A Plio-Pleistocene stack of 57 globally distributed benthic $\delta^{18}O$ records. *Paleoceanography* **20**, (2005).

2. Miller, K. G. et al. High tide of the warm Pliocene: Implications of global sea level for Antarctic deglaciation. *Geology* **40**(5), 407-410 (2012).

3. Milanković, M. M. *Canon of Insolation and Ice Age problem*. Royal Serbian Academy Special Publication (1941).

4. Raymo, M. E., Lisiecki, L. E., & Nisancioglu, K. H. Plio-Plesitocene ice volume, Antarctic Climate, and the global δ^{18}O Record. *Science* **28**, 492-495 (2006).

5. Raymo, M. E., & Huybers, P. Unlocking the mysteries of the ice ages. *Nature* **451**, 284-285 (2008).

6. Huybers, P., & Tziperman, E. Integrated summer insolation forcing and 40,000-year glacial cycles: the perspective from an ice-sheet/energy-balance model. *Paleoceanography* ***23***(1), PA1208 (2008).

7. Naish, T. et al. Obliquity-paced Pliocene West Antarctic ice sheet oscillations. *Nature* **458**(7236), 322-328 (2009).

8. Pollard, D. & DeConto, R. Modeling West Antarctic ice sheet growth and collapse through the past five million years. *Nature* **458**, 329-332 (2009).

9. McKay, R. et al. Antarctic and Southern Ocean influences on late Pliocene global cooling. *PNAS* **109**, 6423-6428 (2012).

10. Lucchi, R. G. et al. Mid-late Pleistocene glacimarine sedimentary processes of a high-latitude, deep-sea sediment drift (Antarctic Peninsula Pacific margin). *Marine Geology* **189**, 343–370 (2002).

11. Tauxe, L. et al. Chronostratigraphic framework for the IODP Expedition 318 cores from the Wilkes Land margin: constraints for paleoceanographic reconstruction. *Paleoceanography* **27**, (2012).

12. Eittreim, S. L., Cooper, A. K. & Wannesson, J. Seismic stratigraphic evidence of ice-sheet advances on the Wilkes Land margin of Antarctica. *Sedimentary Geology* **96**, 131–156 (1995).

13. Anderson, R. F. et al. Wind-driven upwelling in the Southern Ocean and the deglacial rise in atmospheric CO2. *Science* **323**, 1443-1448 (2009).

14. Toggweiler, J. R., Russell, J. L., & Carson, S. R. Midlatitude westerlies, atmospheric CO2, and climate change during the ice ages. *Paleoceanography* **21,** (2006).

15. Cook, C. P. et al. Dynamic behaviour of the East Antarctic Ice Sheet during the Pliocene warmth. *Nature Geoscience* **6**, 765-769 (2013).

16. Depoorter, M. A. et al. Calving fluxes and basal melt rates of Antarctic ice shelves. *Nature* (2013).

17. Mackintosh, A. et al. Retreat of the East Antarctic ice sheet during the last glacial termination. *Nature Geoscience* **4**, 195-202 (2011).

18. Zachos, J et al., Climate Response to Orbital Forcing Across the Oligocene-Miocene Boundary, *Science* **292**, 274-276 (2001).

19. Pälike, H. et al. The heartbeat of the Oligocene climate system. *Science* **314**(5807), 1894-1898 (2006).

20. Kleiven, H.F., Jansen, E., Fronval, T. and Smith, T.M. Intensification of Northern Hemisphere glaciations in the circum Atlantic region (3.5-2.4 Ma) - ice-rafted detritus evidence. Palaeogeo. Palaeoclim. Palaeoecol. **184**(3-4), 213-223 (2002).

21. Williams, G. D., Bindoff, N. L., Marsland, S. J., & Rintoul, S. R. Formation and export of dense shelf water from the Adélie Depression, East Antarctica. *J. Geophys. Res.* **113**, C04039 (2008).

22. Martínez-Garcia, A. et al. Southern Ocean dust-climate coupling over the past four million years. *Nature* **476**, 312-315 (2011).

23. Martinson, D. G., Stammerjohn, S. E., Iannuzzi, R. A., Smith, R. C. & Vernet, M. Western Antarctic Peninsula physical oceanography and spatio-temporal variability. *Deep Sea Res. II* **55**, 1964–1987 (2008).

24. Pritchard, H. D. et al. Antarctic ice-sheet loss driven by basal melting of ice shelves. *Nature* **484**, 502–505 (2012).

25. DeConto, R., Pollard, D., & Harwood, D. Sea ice feedback and Cenozoic evolution of Antarctic climate and ice sheets. *Paleoceanography* **22** (3), (2007).

26. Huybers, P., & Denton, G. Antarctic temperature at orbital timescales controlled by local summer duration. *Nature Geoscience* **1**, 787-792 (2008).

27. Seki, O. et al. Alkenone and boron-based Pliocene pCO2 records. *Earth Planet. Sci. Lett.* **292,** 201-211 (2010).

28. Brigham-Grette, J. et al. Pliocene Warmth, Polar Amplification, and Stepped Pleistocene Cooling Recorded in NE Arctic Russia. Science 340, 1421-1427 (2013).

29. Escutia, C. et al. Circum-Antarctic warming events between 4 and 3.5 Ma recorded in marine sediments from the Prydz Bay (ODP Leg 188) and the Antarctic Peninsula (ODP Leg 178) margins. *Global & Planet. Change* **69**(3), 170-184 (2009).

30. Naafs, B. D. A. et al. Strengthening of North American dust sources during the late Pliocene (2.7 Ma). *Earth & Planet. Sci. Lett.* **317**, 8-19 (2012).

31. IPCC, 2013: *Climate Change 2013: The Physical Science Basis. Contribution of Working Group I to the Fifth Assessment Report of the Intergovernmental Panel on Climate Change* [Stocker, T. F., D. Qin, G.-K. Plattner, M. Tignor, S. K. Allen, J. Boschung, A. Nauels, Y.

Xia, V. Bex and P. M. Midgley (eds.)]. Cambridge University Press, Cambridge, United Kingdom and New York, NY, USA, **in press**.

ACKNOWLEDGEMENTS

This research used samples and data provided by the Integrated Ocean Drilling Program (IODP). The IODP is sponsored by the US National Science Foundation (NSF) and participating countries under the management of Joint Oceanographic Institutions. Financial support for this study was provided to TN and RM from the Royal Society of New Zealand Marsdon Fund Contract VUW0903. Additional support was provided by the Ministry of Science and Innovation (Grant CTM-2011-24079) to CE and FJE.

FIGURE LEGENDS

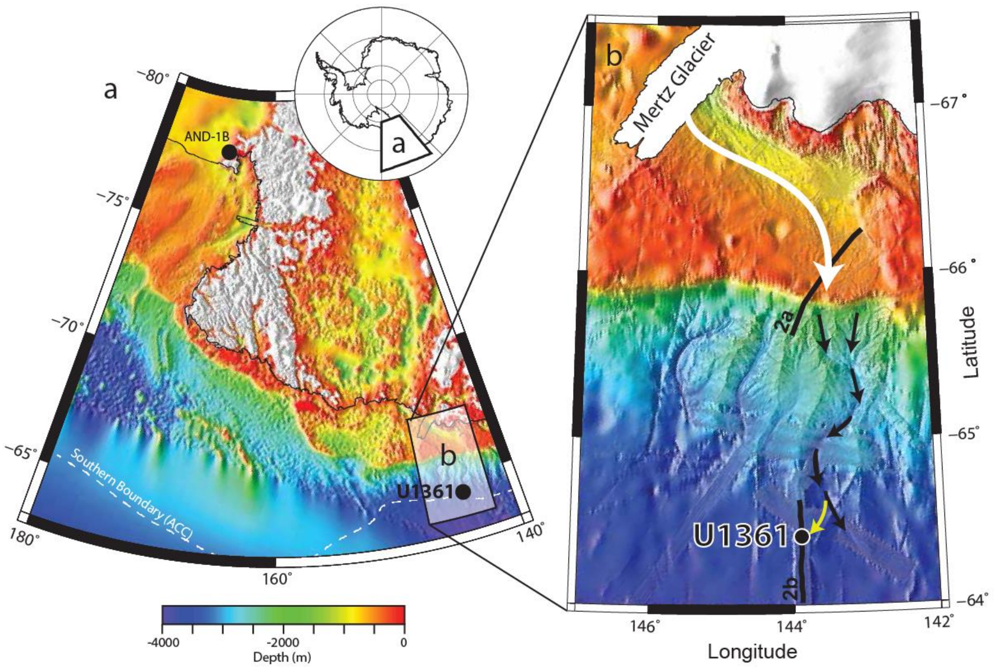

Figure 1. **Location of Site U1361 and bathymetry offshore of the Wilkes Land margin, Antarctica**. Also shown is the location of the Miocene-Plesitocene ANDRILL AND-1B core recovered in the northwestern corner of the Ross Ice Shelf, the southern boundary of the Antarctic Circumpolar Current (ACC), the Mertz Glacier tongue and paleo ice sheet drainage path (white arrows) extending off shore into a slope and rise canyon system. Black lines represent seismic reflection profile tracks represented in Extended Data Figure 1.

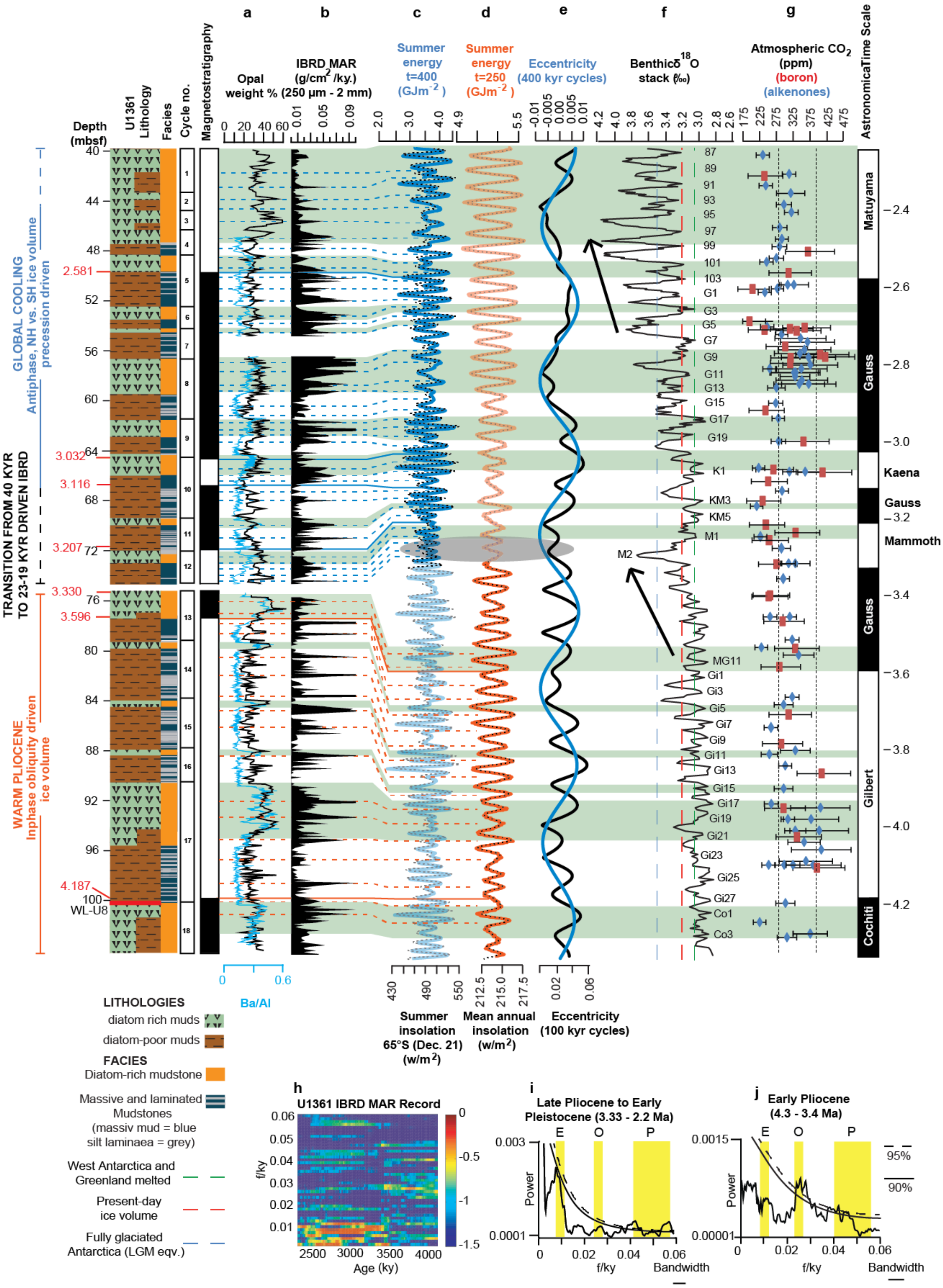

Figure 2. **Depth series developed for IODP site U1361 sediment core between 4.4-2.2Ma of (a) opal percent, (b) IBRD MAR correlated with time series of (c) January insolation**

and total integrated summer energy (where melt threshold [t]=400GJm^{-2}), (d) mean annual insolation and total integrated summer energy (where melt threshold [t]=250GJm^{-2}), (e) eccentricity, and (f) the stacked benthic δ^{18}O record[1]. Also shown is the down core distribution of lithofacies, lithological cycles and magnetic polarity stratigraphy[20]. Maxima in productivity estimates of biogenic opal weight percent and Ba/Al covary with bioturbated/diatom-rich mudstone facies. Grey shaded elipse denotes alignment between a 1.2 Ma node in (d) obliquity modulated mean annual insolation and (e) a 400-kyr minimum in eccentricity which favours polar ice sheet growth and corresponds to (f) a 1‰ glacial δ^{18}O excursion culminating with MIS M2 (arrow). A significant increase in (f) δ^{18}O glacial values from 2.7 Ma (arrow) corresponds with a marked decline in the amplitude of (a) IBRD and a 100ppm decrease in (g) reconstructed atmospheric CO_2 concentration[27]. An (h) evolutive spectrogram of IBRD MAR time series and frequency spectra of (i) Late Pliocene to Early Pleistocene (3.3-2.2Ma) and (j) Early Pliocene (4.3-3.4Ma) IBRD MAR time series show transferral of spectral power from ~40-kyr frequency dominance prior to 3.3Ma to the 100-kyr and 23-19-kyr frequency bands after 3.3Ma.

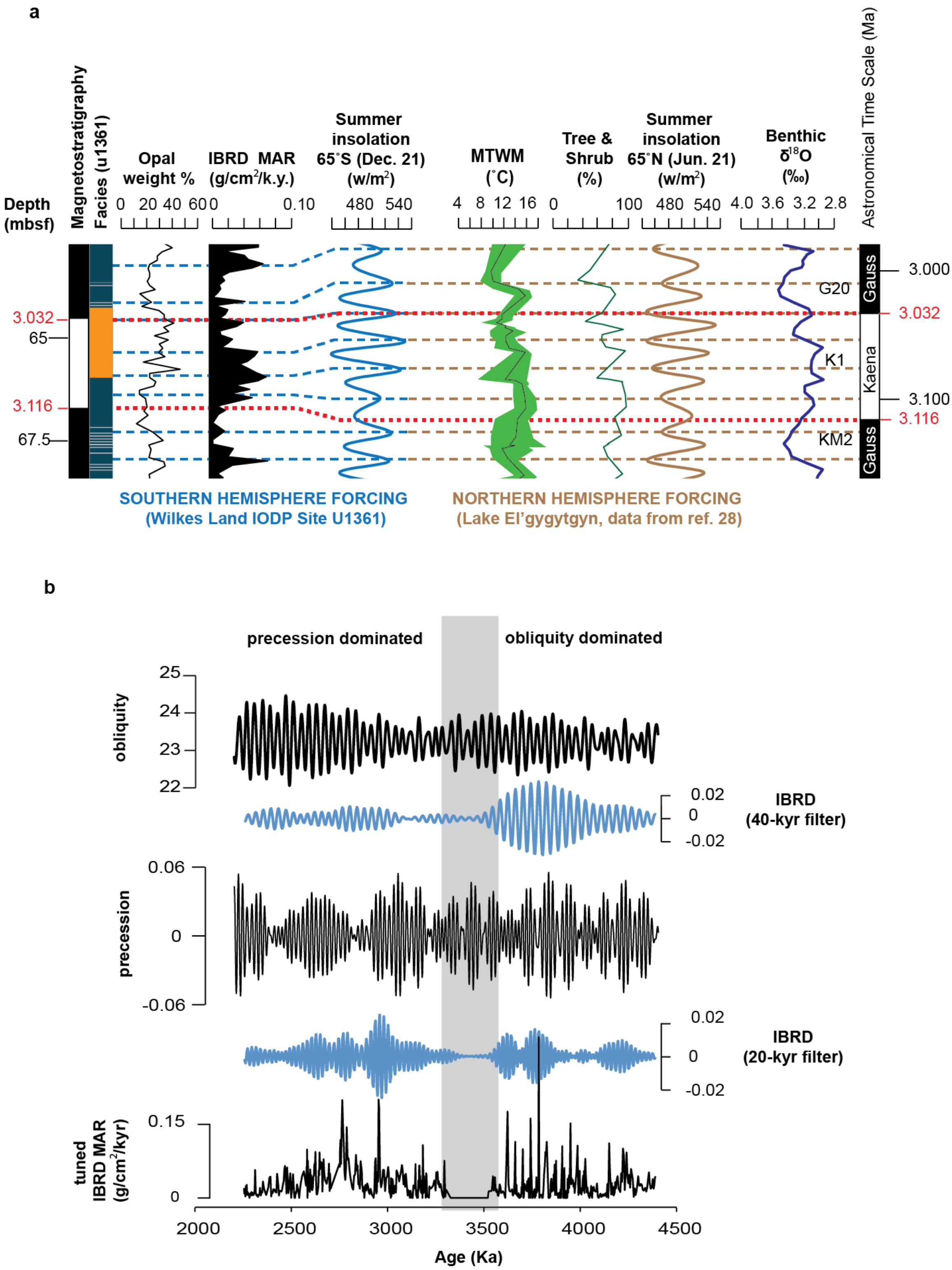

Figure 3. **(a) Corrleation between high-latitude Northern (Lake El’ gygytgyn) and Southern Hemisphere (U1361) climate records synchronised by the Kaena Subchron paleomagnetic reversals illustrates the influence of interhemispheric, anti-phased precision forcing. (b) Tuned IBRD MAR time series for U1361 record with output from**

band-pass filters at precession (20kyr) as well as obliquity (40kyr) frequencies. Grey shading represents a time gap missing from the U1361 record followed by IBRD minima at ~3.3Ma associated with a 1.2 Ma node in obliquity and 400-kyr eccentricity-modulated node in precession.

ONLINE METHODS SECTION

Iceberg Rafted Debris Mass Accumulation Rate calculation

588 samples where processed for grain size and IBRD analysis (Extended Data Table 1). The 250 µm to 2 mm fraction of coarse sand was used to indicate IBRD, as has been used in previous Arctic and Antarctic studies (e.g., ref. 32 and 35). The calculation of an Iceberg Rafted Debris Mass Accumulation Rate (IBRD MAR) followed the methodology used by[32]. As recommended for samples with a mixed biogenic and terrigenous component in that methodology, the >250 µm fraction was dissolved of biogenic silica using 2M NaOH. After biogenic content was dissolved samples were then dry sieved at 150 and 250 µm to 2 mm grain size. Each sample was then examined again under binocular microscope for volcanic ash layers as well as any authigenic minerals, which were absent in all but one sample and was excluded. The MAR of the coarse sand fraction was then estimated using the following equation: IBRD MAR = CS% * DBD * LSR,

where IBRD MAR is the mass accumulation rate ($g/cm^2/k.y.$), CS% is the coarse-sand weight percent, DBD is the dry-bulk density of the nearest value (g/cm^3) and LSR is the interval average linear sedimentation rate (cm/k.y.). The relative abundance of IBRD in the %CS fraction (c.f. ref. 32) was determined the visual examination of every individual sample for authigenic minerals and volcanic ashes, and dissolution of the biogenic component, thus resulting in the CS% being composed entirely of IBRD.

Grain size distribution of the fine-grained (<150 um) material

The fine-grained fraction was recovered by wet sieving at 150 µm followed by the removal of organic material using 30% H_2O_2 and biogenic opal using 2M NaOH. Sampled intervals were analysed for grainsize fractions using a LS 13 320 Laser Diffraction Particle Size Analyzer, using the settings as defined by[36], to correct for the analytical overestimation of the clay fraction (<4 µm). The percent medium-sand fraction (150 to 250 µm) was obtained following wet sieving at 150 µm and dry sieving at 250 µm with biogenic components removed. Biogenic opal weight percent was obtained from dried weights before and after NaOH dissolution during the grain size processing (Extended Data Table 1). This method of opal wt% data carries a degree of analytical uncertainty, as the alkali treatment may also leach clay minerals and volcanic glass. However, comparison to the facies (based on smear slides) and to low-resolution quantitative opal data[15] show identical G/I cyclicity, albeit with an overestimation (10-20%). There is also strong covariance between the opal wt% and the Ba/Al, with any scatter or outliers potentially due to some of opal being the component of the turbidites (some of the silt laminae were diatom-rich[37]) rather than a pure pelagic component.

Identification of iceberg rafted debris versus lag deposits

In order to make the distinction between enrichments in the CS% due to current winnowing of the fine fraction, we determined the sorting parameter[38] of fine grain terrigenous sediment (i.e., biogenic component removed), following the methodology of previous studies recovered from sediment drifts on the continental rise around the Antarctic margin (Extended Data Fig. 4)[39]. IBRD peaks coinciding with well-sorted terrigenous material are likely to be a concentration of coarse material following winnowing of fine-grained sediments by higher energy bottom currents. Whereas, IBRD peaks correlating with poorly to very-poorly sorted material reflect actual IBRD events superimposed onto the background hemipelagic sedimentation. Furthermore, peaks of well-sorted terrigenous material also serve to identify potential hiatuses between the chronostratigraphic tiepoints (i.e., magnetic reversals) in our record related to current winnowing[39]. There is a complete absence of well-sorted material in all samples anaylsed, further supporting our assumption of no major hiatuses in the studied interval. All IBRD peaks coincide with poorly to very-poorly sorted sediment, indicating IBRD events are not the product of lag deposits and the lack of moderately- to well-sorted terrigenous sediment indicates bottom current energy was never high enough energy for erosion to dominate over deposition. Along-slope currents are also unlikely to have a major erosive control, with modern-day bottom currents flowing eastward across the drill site at a velocity of 1.8-6.6 cms^{-1} [40], which is well-below the current strength required for the onset of selective deposition (10-12cms^{-1}) or extensive winnowing of the fine fraction (>20cm s^{-1})[41]. Downslope currents, resulting from High Salinty Shelf Water masses passing down the continental rise, are also low-energy throughout the Plio-Pleistocene in these distal levee environments along the Wilkes Land margin[42,43].

Iceberg Rafted Debris as proxy

As the Antarctic ice sheets lose 50-80% of their mass from iceberg calving[16], significant changes in the mass balance of marine-based ice sheet should be evident in high-quality IBRD records, provided certain caveats are considered.

We have demonstrated that the untuned IBRD contains a statistically significant signal at orbital periodicities throughout the record (Fig. 2), therefore, suggesting iceberg calving is not a random process at this scale. Orbital pacing has also been qualitatively implied by previous studies along the EAIS margin, but these studies did not statistically identify the frequencies of that pacing as well as the variance between the 40-kyr and 20-kyr cycles[29,39]. While late Pleistocene studies of Antarctic sediment cores display a glacial to interglacial cyclicity, with peaks in IBRD occurring during deglaciation and interglacials, these records can reflect distinct regional differences in ice sheet response to glacial-interglacial processes, including bottom current winnowing and changes in sedimentation rates (e.g., ref. 44). We have assessed the influence both of these processes in U1361 in the main text as well as above, and we are confident that they are not a major influence on the IBRD record.

Another important consideration is that Antarctica's larger ice shelves lack basal debris (i.e., Ross Ice Shelf), which melts out close to the grounding line, and consequently does not distribute abundant amounts of ice rafted debris to the ocean. However, smaller ice shelves and ice tongues source sediment-laden icebergs containing significant basal debris layers[45]. Thus, we interpret the U1361 record to reflect IBRD from the calving of sediment-laden bergs from outlet glaciers draining the EAIS (either the Ross Sea or Wilkes Land margin). However, we stress this does not exclude the presence of local ice shelves which may have played an important role in buttressing the grounded ice sheet, particularly during glacial periods. Thus, if there was a signficant ice shelf contribution to our record (i.e., low IBRD = fringing ice shelves; high IBRD = non fringing ice shelves), then this is directly relevant to assessing changes in dynamical ice discharge. Also, large ice shelves (such as the Ross Ice Shelf) may not have persisted through glacial minima in the Pliocene (e.g., the AND-1B record[7,8]). Thus, an alternative explanation for the decrease in IBRD MAR after 2.5 Ma, or during nodes in precession and obliquity, may reflect increased persistence or duration of large fringing ice shelf shelves (and thus "cleaner" icebergs) during these colder intervals, which in turn would have restricted dynamical ice discharge.

Changes in surface ocean currents are unlikely to have influenced iceberg drift patterns at U1361. The dominant easterly flow over the site (Antarctic Coastal Current and its associated front - Antarctic Slope Front) is unlikely to have changed direction, due to bathymetric (i.e., the continental rise/shelf break) and geostrophic considerations, as demonstrated under the scenarios of a greatly reduced EAIS[25]. IBRD peaks from further in the Southern Ocean (e.g., polar front) may represent glacial maxima as icebergs can survive for longer time periods in the colder glacial period waters. However, U1361 is proximal enough to outlet glaciers of the Antarctic margin for smaller "dirty" icebergs derived from these sources to survive moderate levels of SST warming (as inferred for the Pliocene), but not so close as to be influenced by a single outlet glacier, or a single iceberg dumping[46]. The 3500m water depth and open ocean location of U1361 (with only seasonal winter sea) means icebergs would never be "locked in" place over the drill site, and would pass over the drill site very rapidly (i.e., minutes as they do today).

XRF Ba/Al analysis

The bulk major element composition was measured between cores U1361A-6H to 11H using an Aavatech TMX-ray fluorescence (XRF-Scanner) core scanner at the IODP-Core Respository/ Texas A&M University laboratories (USA). Non-destructive XRF core-scanning measurements were performed at 10 kV in order to measure the relative content of elements ranging from aluminum (Al) to barium (Ba). Measurements were acquired every 5cm. In addition, discrete samples were taken to measure Ba and Al by X-Ray Fluorescence (XRF) using pressed pellets prepared by pressing about 5 g of ground bulk sediment into a briquet with boric acid backing. The quality of the analysis was monitored with reference materials showing high precision with 1 sigma 1.0e3.4% on 16 data-sets at the 95%

confidence level. For XRF 42 samples were selected in a 20 m representative interval (47 to 67 mbsf) at ~40-60 cm intervals. Compared Ba and Al trends using both techniques are virtually identical and indicate that obtained XRF-Scanner data are robust and reliable.

Age Model

The age model for the U1361 record was developed by an integration of biostratigraphic datums (diatom, radiolarian, calcareous nannofossils and dinoflagellate cyst) and a magnetic polarity zonation[11]. We used the biostratigraphically-constrained magnetostratigraphic tie points for correlations between the IBRD MAR record presented in this study and orbital paramters as well as the benthic $\delta^{18}O$ stack[1]. The age model of U1361 highlights the continuous nature of the Plio-Pleistocene interval in the U1361 record (Extended Data Fig. 5) with long-term sedimentation rates estimated at ~30 m/m.y., with no major time gaps due to erosion. However, a single condensed interval is identified around 3.3 Ma (~74.52 mbsf) (Fig. 2; Extended Data Fig. 5). The Early Pliocene from ~4.2 Ma to Early Pleistocene at ~2.0 Ma contains no major core disturbances with only one major core gap extending between ~3.6 to ~3.33 Ma[37]. The continuous and uniform nature of the Plio-Pleistocene sedimentation rates in U1361, combined with the detailed grain size anaylses discussed above indicates that winnowing is not a major influence on sedimentation at this site.

Frequency Analysis

Using the age model[11] we performed evolutionary spectral analysis in Matlab© (using a spectrogram function developed by Peter Huybers and available at his website http://www.people.fas.harvard.edu/~phuybers/Mfiles/index.html). This was followed by power spectral analysis using the SSA-MTM toolkit for the Multi-Taper method (MTM) analysis[33] with five data tapers for the untuned IBRD MAR (Fig. 2; Extended Data Fig. 6) and biogenic opal weight percent (Extended Data Fig. 7) time series at 3 kyr resolution for the Early Pliocene and 4 kyr resolution for the Late Pliocene-Early Pleistocene. Equal time spacing was achieved by linear interpolation based on average temporal sample spacing of time series segments as there is a gap in our data exceeding 100 kyrs that predates 3.33 Ma. The statistical significance of spectral peaks was tested relative to the null hypothesis of a robust red noise background, AR(1) modelling of median smoothing, at a confidence level of 90% and 95%[34]. Raw (AR1) models with a harmonic reshape set to a 90% threshold were used to test the comparative variance in obliquity versus precession (Extended Data Fig. 6).

Tuning of the IBRD MAR record and bandpass filtering was conducted in Analyseries[47] and filters for obliquity (central frequency of 0.025, bandwidth of 0.003) and precession (central frequency of 0.045, bandwidth of 0.005) applied (Fig. 3b). Following tuning, power spectra was carried out using the same parameters with the SSA-MTM toolkit as the untuned data (Extended Data Fig. 7).

SUPPLEMENTARY INFORMATION

Sedimentology Discussion

Lithofacies

Grain size data collected on Pliocene and Early Pleistocene intervals of U1361 confirm the lithofacies descriptions conducted by the shipboard scientific party[37] (Extended Data Fig. 2, 3). The bioturbated Diatom-Rich/Bearing Mudstone (Extended Data Fig. 2 and 3a-b) is a light greenish grey silty clay with >25% diatoms in smear slides from lithological descriptions, and > 25 wt% biogenic opal via NaOH dissolution. IBRD is common throughout and values of Ba/Al, a productivity indicator[48], are high throughout and correlate well with biogenic opal weight percents (Extended Data Fig. 8). This facies is directly equivalent to Facies D in the initial reports volume of Exp. 318 Site U1361[37].

The Massive and Laminated Mudstone (Extended Data Fig. 3c-d) is olive grey and massive in structure but contains packages of mm- to cm-scale silt and fine sand laminations, variable bioturbation and mm-size silt lenses. Silt laminae/beds are internally massive, contain sharp bases with a range from 1.3 mm to 2.5 cm in thickness with the mean thickness 4.5 mm, and laminae exceeding 1 cm in thickness (i.e. beds) are rare (<5% of all silt laminae/beds). Diatom content is relatively poor throughout (<25 wt% biogenic opal) while IBRD is common throughout.

Facies interpretation

The facies assemblages in the Pliocene-Early Pleistocene interval of U1361 are consistent with existing facies models of sedimentation in distal channel-levee systems on the lower continental rise from other regions globally[49] and from the Antarctic margin[10,43,50,51,52,53]. The presence of normally graded well-sorted mm-scale silt laminae and lenses in otherwise massive mudstones with sharp bases, but no internal structures or IBRD is consistent with deposition by non-erosive spill-over of low density turbidite deposits onto a channel levee in a distal lower continental rise setting (e.g. Ref. 10, 43, and 56). The laminae themselves lack IBRD and bioturbation indicating relatively rapid deposition. Thus, the characteristics of these laminae argue against a traction current (i.e. winnowing) origin of deposition[10,43,56]. We also note the relationship between these laminae intervals of mudstones are identical in nature to the mud turbidite facies (Extended Data Fig. 3c) “T3” to “T7” beds[57], representing base-cut-out sequences and deposition in a low-density turbidity current by overflow on the distal levee setting – i.e. a non-erosional depositional setting compared to more proximal settings[43,56]. The presence of IBRD and bioturbation within intervals of the massive mudstone facies, suggests that turbidite intervals where deposited by numerous events over a relatively prolonged period, rather than a singular event.

A lull or reduction in persistent turbidity current activity is represented by the presence of the bioturbated diatom-rich/bearing mudstone, consistent with the Pelagite/Hemipelagite “F” beds[56]. Grain size analyses reveal that the bioturbated Diatom-Rich/Bearing Mudstone facies are coarser (i.e., silty clays) than the massive mudstone intervals (distinct silt laminae were excluded from this analysis) (Extended Data Fig. 2 and 3). The coarse nature of the bioturbated diatom rich/bearing facies deposits implies reworking of older turbidites[41] (i.e. silt laminae and clays) and homogenization to a silty clay texture as a result of bioturbation and bottom current processes between sediment gravity flow events. The lack of erosional surfaces or coarse sands/gravel layers (i.e. lag surfaces) suggests that although low-energy bottom currents or bioturbation acted to remobilize fine-grained sediment, depositional processes dominated over erosional events.

However, in the Early Pleistocene (e.g., above 48 mbsf) bioturbation of diatom-rich mudstones are distinguished by an overall decrease in IBRD, and an increase in overall silt abundance displaying a gradual coarsening upwards (i.e. reverse grading) at the m-scale (Extended Data Fig. 2c) and slight decrease in the long-term sedimentation rate (~2.33 cm/k.y.) compared with the Pliocene section (~3.10 cm/k.y.). Silt laminae become notably rarer and less laterally continuous above 47.57 mbsf (Fig. 2), with only 57 laminae recorded between 47.57 and 0 mbsf compared to 278 between 100 and 47.57 mbsf. Although distinct continuous laminae are lacking, silt lenses and silt mottles are common and often display an irregular alignment (Extended Data Fig. 2a). Combined, the textural characteristics, reverse grading, and the sedimentary structures are consistent with silty-sandy contourite facies or, more specifically for site U1361, bottom-current reworking[56 Fig. 9]. In areas influenced by active polynyas, bottom-current influenced sediments are highly bioturbated with irregularly aligned silt lenses and mottles in which boundaries between different sediment layers become difficult to distinguish[55]. This is interpreted to be consequence of the low-energy downslope delivery of highly oxygenated and nutrient rich waters formed off the margin within active polynya systems resulting in sediments containing high biogenic content and benthic activity. In contrast, other regions in Antarctica not influenced by an active polynya system are charactersied by anoxic conditions result in bottom-current influenced sediments of hemipelagic grey muds with well-defined laminae that are rhythmic in nature, continuous, lack bioturbation, contain low biogenic content, and contain sparse IRD or pebbly layers[43,55]. Thus, we have interpreted the reverse grading above ~48 mbsf, sparse IBRD, highly bioturbated sediment with irregular alignment of silt lenses and mottles as representing colder glacial conditions (in which events of sediment-laden iceberg discharge become rare) with downslope currents due to enhanced polynya mixing off the Wilkes Land margin increases the delivery of oxygenated nutrient rich water to the lower continental rise, increasing both bioturbation and bottom current strength[43,55].

Seismic stratigraphic interpretation of existing multichannel reflection seismic profiles crossing Site U1361 (Extended Data Fig. 1) provide further evidence that the dominant sedimentary processes building these more distal levees is the fine-grained components of turbidity flows traveling through the channel (where erosion does occur) and from inter- and over-flow depositing sediment as hemipelagic drapes. Although, sediment waves are observed locally in seismic lines from the lower rise that are perpendicular to the margin (downslope processes), these are within the overbank deposits and are smooth (i.e., very low-relief) indicating that bottom-currents are not a dominant process at this distal site. In contrast, sediment waves are very well-developed in older sequences (i.e., phase 2 of ref. 56), of upper Oligocene-Miocence age[37] in the lower continental rise and in more proximal continental rise areas (i.e., where Site U1359 is located) suggesting a mixed turbidite and bottom-current deposition[56,57,58]. It is during this time that the large levees and ridges form on the Wilkes Land continental margin[37]. The change from sedimentation dominated by mixed turbidite and bottom-current deposition (Phase 2) to sedimentation dominated by turbidite & hemipelagic deposition (section containing sediments considered in this study) coincides with a shift in sedimentary depocenters from the continental rise to the continental shelf[57]. Instead of large levee deposits, low-relief overbank deposits spilling from the channels are commonly observed on-lapping the previous levees and ridges[56,57].

Identification of glacial to interglacial sedimentation processes

We interpret the massive/laminated mudstone facies as being predominately deposited during periods of glacial maxima, with large volumes of unconsolidated sediment being delivered to the continental shelf edge either through the deposition of till deltas or via bedload rich turbid glacial melt water plumes during grounding line advance[10,12,42,59,61] with turbidity current initiation due to slope failures on oversteepened foreset strata. This interpretation is supported by seismic profiles that indicate glacial advances occurred regularly since the Early Pliocene, as evinced by the onset of steeply dipping foresets and the development of the modern progradational wedge above seismic unconformity WL-U8 which can be traced from the continental shelf to rise and dated at 4.2 Ma (~100 mbsf) in U1361[11,12,42] (Extended Data Fig. 1). Steeply dipping foresets are commonly found around the margin of the Antarctic and are interpreted as being deposited in a proglacial setting at the grounding line of ice streams, and are therefore a direct result of glacial advances to the shelf edge [12,45,61,62].

We interprete the Diatom-Rich/Bearing Mudstone facies with IBRD and pervasive bioturbation throughout to be predominately deposited during glacial minima. This interpretation is supported by a recent isotopic Nd and Sr provenance study of the fine-grained fraction in the Pliocene interval of the U1361 core and indicate that the eroding margin of the EAIS had receded up to several 100 km inland[15]. The interplay of bioturbation and downslope along slope currents results in an overall increase in the silt component, most likely due to homogenization of sediment texture and removal of primary sedimentary structures (i.e., silt laminae) within these intervals. Turbidity currents may have still been delivering sediment during these intervals, perhaps as the consequence of isostatic adjustments during postglacial retreats[42] or initiated by hypersaline density flows of high salinity shelf waters passing down the continental rise. However, the homogenization of these sediments suggests that turbidity current activity may have been less frequent. Reduced turbidity current activity does not explain these facies alone, as changes in biogenic opal weight percent covary with Ba/Al measurements within these diatom-rich/bearing intervals (Extended Data Fig. 8). Thus, we interpret these intervals as representing times of enhanced biogenic activity in the surface waters above the drill site, accompanied by a reduction in turbidity current activity. We also note that during the Holocene, most fine grained sediment is advected towards the inner continental shelf in the Mertz-Ninnis tough rather than towards the shelf edge[63], due to the reverse slope morphology of the continental shelf that developed in the Early Pliocene (i.e., above WL-U8), and thus it is likely this was also situation for Late Pliocene-Pleistocene glacial minima[12].

The modern day position of the Southern Boundary of the ACC is ~10 km to the north of Site U1361[64], and is the location of the Antarctic Divergence where relatively warm UCDW upwells and biological productivity is high. Sea surface temperatures (SST) reconstructions indicate that the Southern Ocean was up to +4°C warmer[65] with a significantly reduced sea ice field during the warmest Pliocene in the Ross Sea[9], Prydz Bay[29],[66] and Antarctic Peninsula[66] regions. For interglacial times, connections have been made between southward zonal shifts in the intensity or location of southern westerlies and their influence on incursions of CDW or modified CDW (MCDW) (when some mixing with Antarctic waters has occurred) onto the continental shelves around Antarctica, with consequences for the melting of the marine margins of the ice sheets[7,9,13,14,24,68]. However, the main dynamical barrier for CDW (or MCDW) in Wilkes Land is the Antarctic Slope Front (at the shelf break/upper continental rise), which creates a "V-shaped" isopyncial that extends into intermediate water depths and restricts CDW incursions onto the continental shelf. Thus, changes in the location, intensity or vigour of this current, related to the strength or location of the zonal polar winds (i.e., polar easterlies and the subpolar westerlies), directly regulates MCDW incursion, more so than a direct bathymetric control[21].

Early Pleistocene diatom-rich/bearing muds above ~48 mbsf, while displaying similarities to Pliocene intervals, are distinctively different in IBRD content, arrangement in silt lenses and mottles as well as displaying an apparent overall negative grading. The Early Pleistocene intervals reflect reworking by downslope bottom currents in which enhanced delivery of oxygenated and nutrient-rich waters formed in the Mertz Polynya promoting productivity and bioturbation. Silt lenses and mottles appear more irregularly aligned suggesting more vigourous bottom current remobilization of fine grain clay sediments, but the lack of significant winnowing indicates these currents were still low energy. Sparse IBRD suggests lulls in iceberg calving as disintegration events become less frequent as the ice sheet stabilized and begins to fluctuate at the same extent as the Late Pleistocene glacial cycles. These bottom currents appear to be related to low-energy downslope (rather than alongslope currents), on account of the seismic data and modern oceanographic current data discussed earlier. Continental rise channels (like the Jussieu channel) act as conduits for the delivery of cascading high-salinity shelf water to the rise, however, these currents are low-energy and appear non-erosived in this distal low-relief levee setting[43,69].

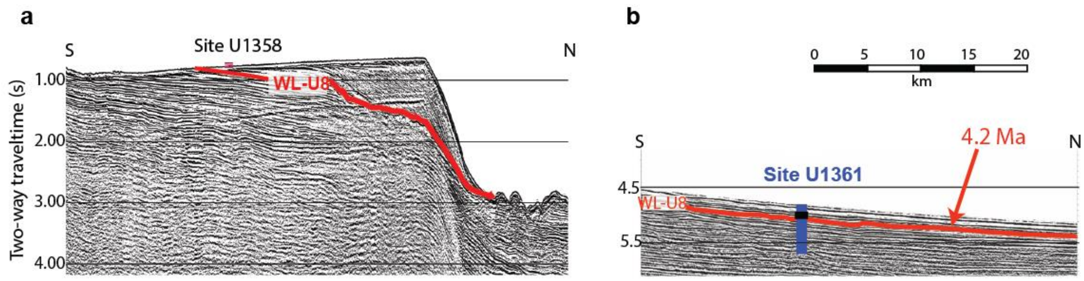

Extended Data Figure 1. Seismic reflection profiles of Wilkes Land continental shelf and Rise. Interpreted seismic unconformity WL-U8 is highlighted in red extending from the continental shelf (a) to the rise (b) with Site U1361 identified in blue. WL-U8 is age dated to 4.2 Ma[11,57].

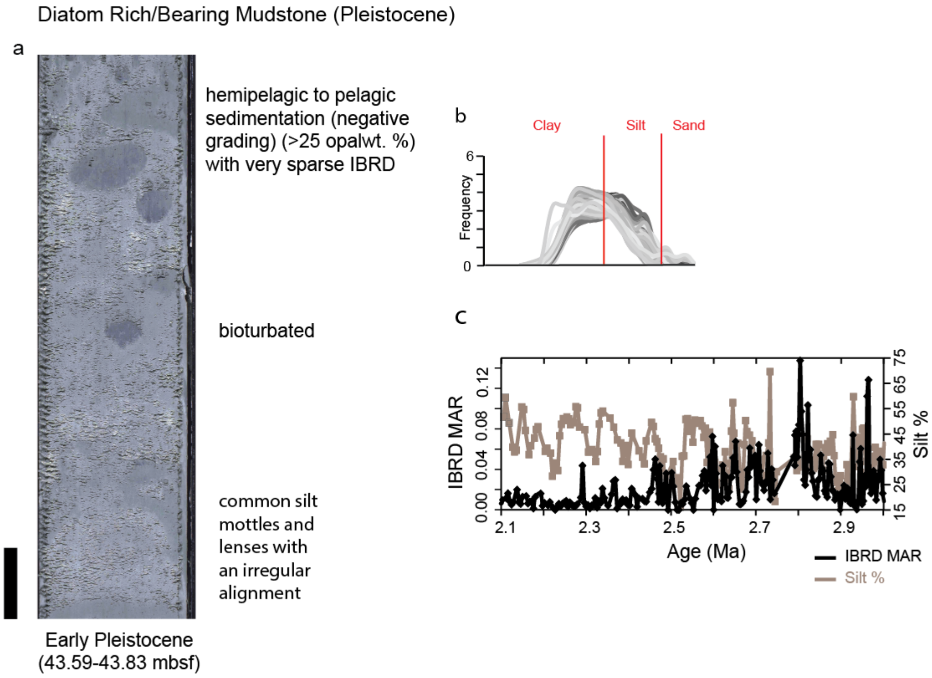

Extended Data Figure 2. (a) Representative photo highlighting distinct sediment characteristics of Early Pleistocene Diatom Rich/Bearing Mudstone lithofacies. Black scale bar represents 3 cm. (b) Grain size frequencies of representative samples are displayed. (c) Draw down in Early Pleistocene IBRD coinciding with an overall increase in silt content.

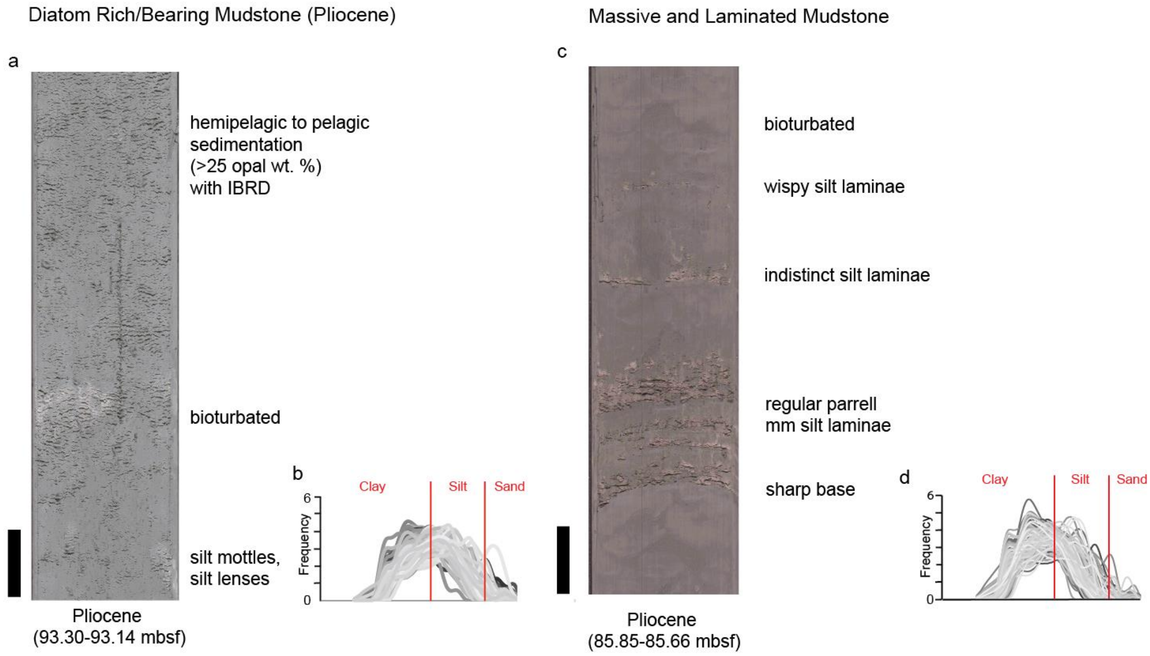

Extended Data Figure 3. (a) Representative photo with (b) grain size frequencies highlighting distinct sediment characteristics of Pliocene Diatom Rich/Bearing Mudstone and (c-d) the Massive and Laminated Mudstone lithofacies. Black scale bar represents 3 cm.

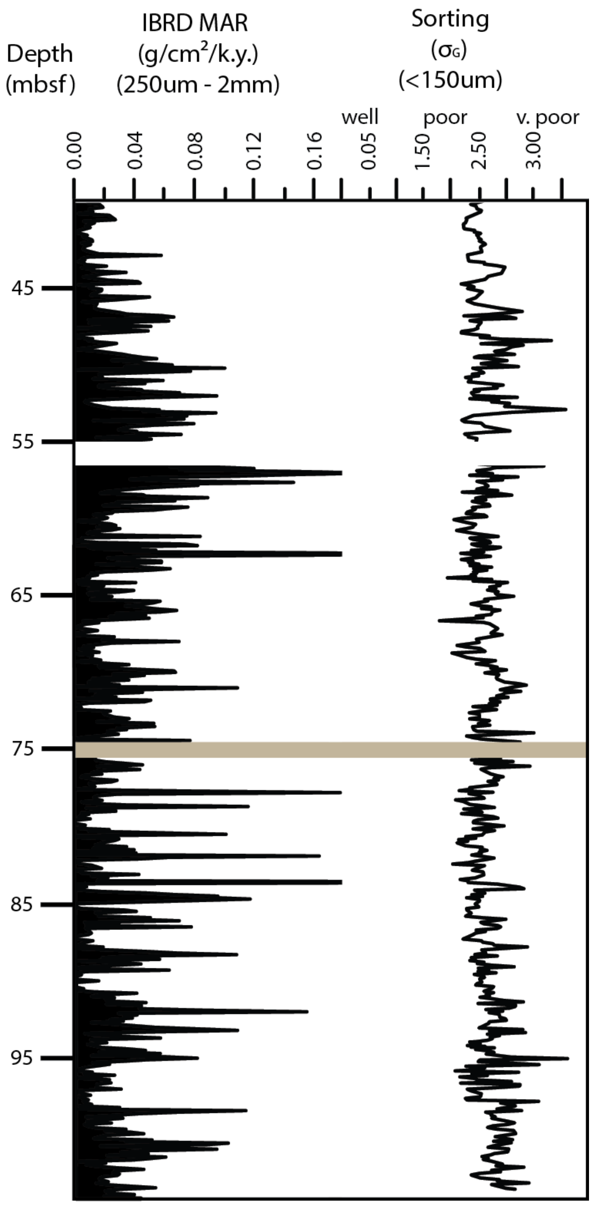

Extended Data Figure 4. U1361 IBRD MAR compared to sorting of fine grained (<150 µm) terrigenous material. Sorting measurements follow parameters defined by[38]. All samples are classified as being very poorly (2-4σ) sorted. Grey bar indicates core break.

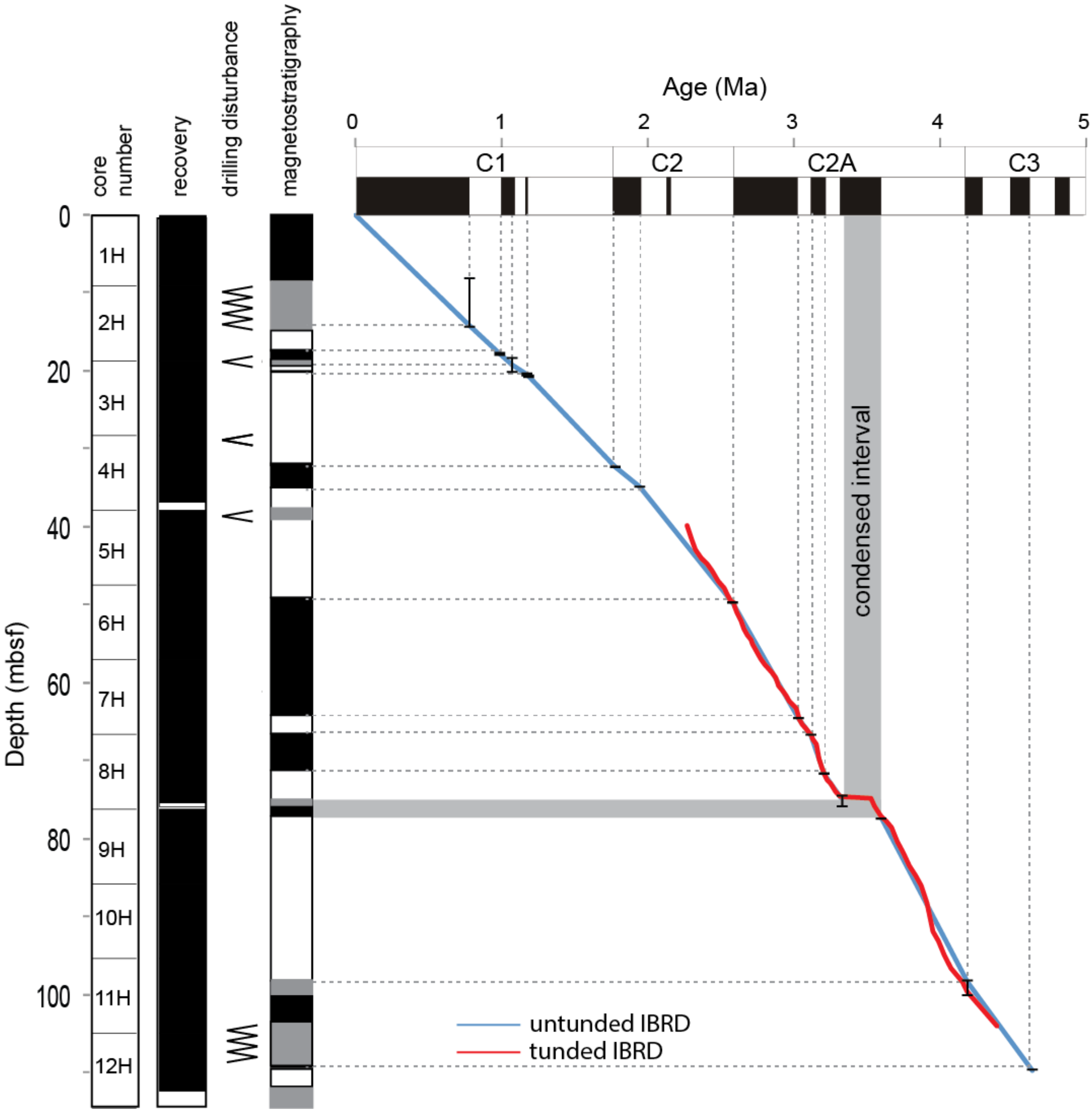

Extended Data Figure 5. Age-dpeth plot and magnetostratigraphic tie points for the Pliocene-Pleistocene record of U1361. The condensed interval around ~3.3 Ma is highlighted in grey. Error bars mark uncertainty the stratigraphic location of polarity reversal boundaries in the U1361 core after ref 21. Also displayed is core recovery and disturbance.

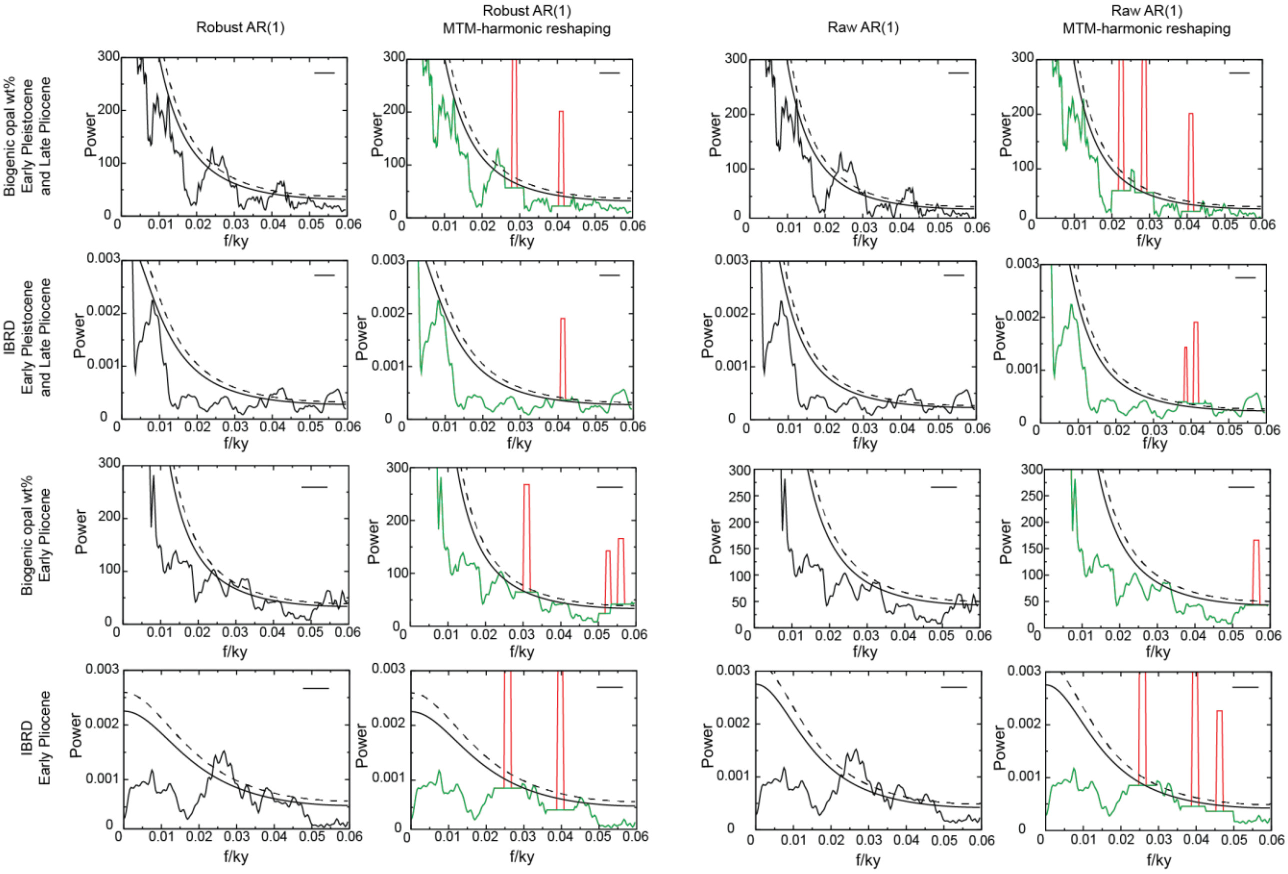

Extended Data Figure 6. Power spectra using Robust and Raw AR(1) red noise background. Raw data output is represented in black lines, while harmonic reshaping data output set to a 90% threshold is represented with green lines in which red lines highlight harmonics. Statistical significance is noted at 90% (solid black line) and 95% (dashed black line).

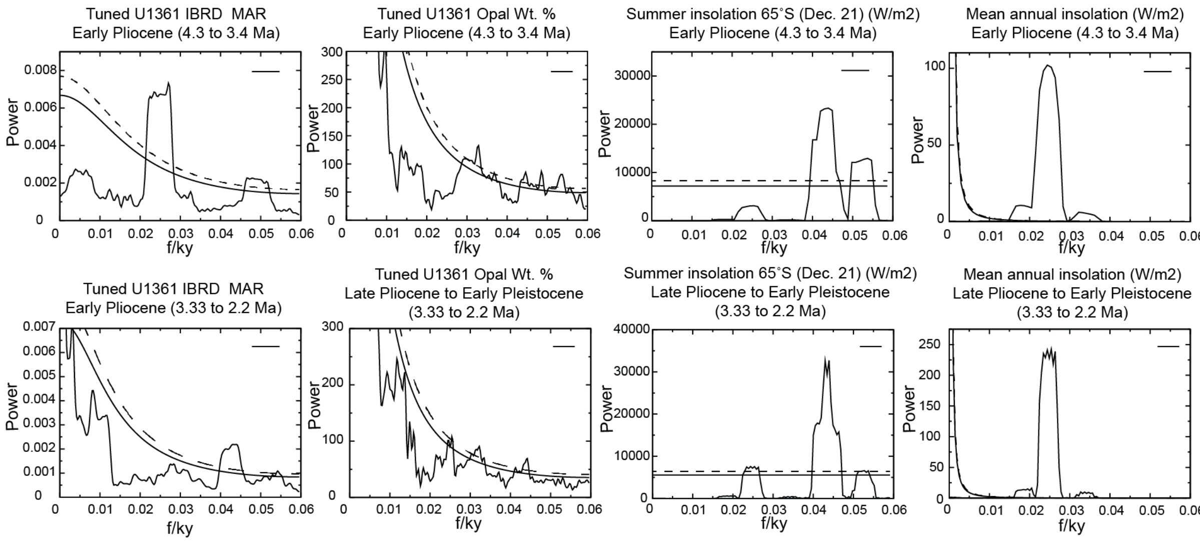

Extended Data Figure 7. Power spectra using the IBRD tuned age model. Early Pliocene IBRD MAR and mean annual insolation display strong 40 kyr cycles of obliquity while biogenic opal does not display Milankovitch orbital frequencies. Late Pliocene-Early Pleistocene IBRD MAR and summer insolation display strong 23 and 19 kyr cycles of precession while biogenic opal wt. % only contains less distinct precession frequencies with 40 kyr obliquity significance. Statistical significance is noted at 90% (solid black line) and 95% (dashed black line).

Extended Data Table 2. Antarctic-Arctic[28] precession-paced climate phase relationship. Synchronised by the timing of the top and bottom Kaena Subchron paleomagnetic reversals.

P-mag boundary	Age (Ma)	Insolation 65°N (w/m2)	Insolation 65°S (w/m2)	U1361 Wilkes Land proxy	Antarctic U1361 climate	Lake El'gygytgyn proxy	Arctic Lake E climate
Top Kaena	3.032	Low (443.24)	High (535.22)	Peak opal* Peak Ba/Al High IBRD* Diatom-rich*	Sea-ice free, productive warm open ocean during summer with ice berg rafting	Low opal Low Si/Ti Low trees and shrubs index* Low MTWM* Low precipitation index	Cool, dry summers Low lake productivity Cold deciduous forest
Base Kaena	3.116	High (509.84)	Low (479.43)	Low opal* Low Ba/Al Low IBRD* Diatom-poor*	Sea-ice covered, non-productive cold ocean during summer with limited ice berg rafting	High opal High Si/Ti High trees and shrubs Index* High MTWM* Increased precipitation index	Warmer, wetter summers Increased lake productivity Cool conifer mixed forest

***** Data displayed in Fig. 3a.

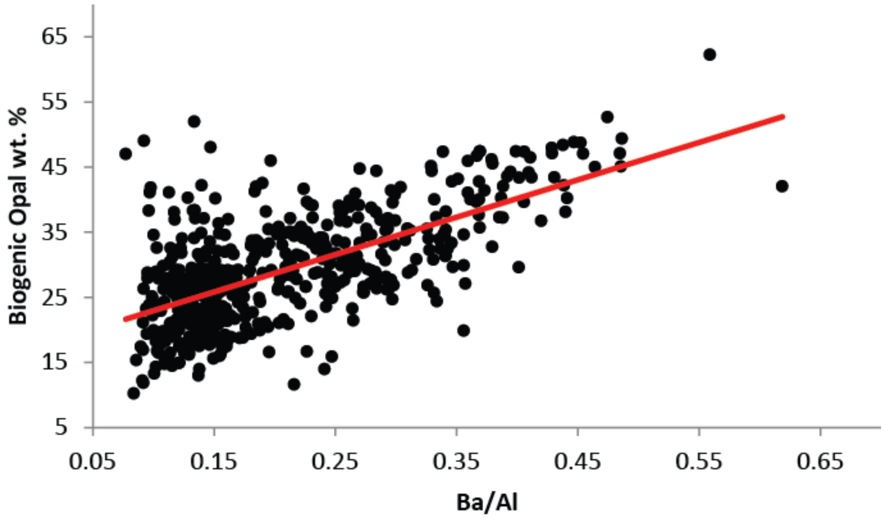

Extended Data Figure 8. Cross plot of U1361 biogenic opal wt. % and Ba/Al. Linear interpolated at 3 kyr resolution of biogenic opal wt. % and Ba/Al with r = 0.65 and p value of 0.00.

Supplementary References

32. Krissek, L, A. 11. Late Cenozoic ice-rafting records from Leg 145 sites in the north Pacfic: Late Miocene onset, Late Pliocene intensification and Pliocene-Pleistocene events. *Proc. Ocean Drill. Program, Sci. Results* **145**, 179-194 (1995).

33. Ghil, M. et al. Advanced spectral methods for climatic time series. *Rev. Geophys.* **40**(1), (2002).

34. Mann, M. E., & Lees, J. M. Robust estimation of background noise and signal detection in climatic time series. *Climatic Change* **33**(3), 409-445 (1996).

35. Cowan, E. A., Hillenbrand, C-D., Hasslet L. E., & Ake, M. T. Coarse-grained terrigenous sediment deoposition on continental rise drifts: A record of Plio-Pleistocene glaciation on the Antarctic Peninsula. *Palaeogeogr. Palaeoclimatol. Palaeoecol.* **265**(3-4), 275-291 (2008).

36. Sperazza, M., Moore, J. N., & Hendrix, M. S. High-resolution particle size analysis of naturally occurring very fine-grained sediment through laser diffractometry. *J. Sediment. Res.* **74**(5), 736-743 (2004).

37. Escutia, C., Brinkhuis, H., Klaus, A., & Expedition 318 Scientists. Site U1361. *Proc. Integrat. Ocean Drill. Program* **318**, 1-57 (2011).

38. Folk, R. L., & Ward, W. C. Brazos River bar [Texas]; a study in the significance of grain size parameters. *J. Sediment. Res.* **27**, 3-26 (1957).

39. Passchier, S. Linkage between East Antarctic Ice Sheet extent and Southern Ocean temperatures based on Pliocene high-resolution record of ice-rafted debris off Prdyz Bay, East Antarctica, *Paleoceanography* **26,** (2011).

40. Bindoff, N. L., Rosenberg, M. A., & Warner, M. J. On the circulation and water masses over the Antarctic continental slope and rise between 80 and 150°E. *Deep Sea Res. II* **47**(12-13), 2299-2326 (2000).

41. McCave, I. N., & Hall, I. R. Size sorting in marine muds: Processes, pitfalls, and prospects for paleoflow-speed proxies. *Geochem. Geophys. Geosyst.* **7**(10), 1-37 (2006).

42. Escutia, C. et al. Cenozoic ice sheet history from east Antarctic Wilkes Land continental margin sediments. *Global Planet. Change* **45**(1-3), 51-81 (2005).

43. Caburlotto, A. et al. Sedimentary processes on the Wilkes Land continental rise reflect changes in glacial dynamic and bottom water flow. *Int. J. Earth Sci.* **99**, 909-926 (2010).

44. Ó'Cofaigh, C., Dowdeswell, J. A., & Pudsey, C. J. Late Quaternary iceberg rafting along the Antarctic Peninsula continental rise and in the Weddell and Scotia Seas. *Quaternary Research* **56**(3), 308-321 (2001).

45. Anderson, J. B. *Antarctic Marine Geology*. Cambridge University Press, Cambridge. (1999).

46. Stuart, K. M., & Long, D. G. Tracking large tabular icebergs using the SeaWinds Ku-band microwave scatterometer. *Deep Sea Res. Part II* **58**(11), 1285-1300 (2011).

47. Paillard, D, Labeyrie, L., & Yiou, P. Macintosh program performs time-series analysis. *Eos, Trans. Amer. Geophys. Union* **77**(39), 379 (1996).

48. Dymond, J., Suess, E. and Lyle, M. Barium in deep-sea sediment: a geochemical proxy for paleoproductivity. *Paleoceanography* **7**(2), 163-182 (1992).

49. Stow, D. A. V., & Piper, D. J. W. Deep-water fine grained sedimentsL facies models, in Fine-Grained Sediments: Deep-Water Processes and Facies. *Geol. Soc. Spec. Publ.*, **15**(1), 611-646 (1984).

50. Gilbert, I. M., Pudsey, C. J., & Murray, J. W. A sediment record of cyclic bottom-current variability from the northwest Weddell Sea. *Sedimentary geology* **115**(1), 185-214 ***(***1998).

51. Pudsey, C. J., & Camerlenghi, A. Glacial–interglacial deposition on a sediment drift on the Pacific margin of the Antarctic Peninsula. *Antarctic Science* **10**, 286-308 (1998).

52. Pudsey, C. J. Sedimentation on the continental rise west of the Antarctic Peninsula over the last three glacial cycles. *Marine Geology* **167**(3), 313-338 (2000).

53. Busetti, M. et al. Plio-Quaternary sedimentation on the Wilkes land continental rise: preliminary results. *Deep Sea Res. Part II* **50**(8-9), 1529-1562 (2003).

54. Hepp, D. A., Mörz, T., & Grützner, J. Pliocene glacial cyclicity in a deep-sea sediment drift (Antarctic Peninsula Pacific Margin). *Palaeogeogr. Palaeoclimat. Palaeoecol.* **231**, 181-198 (2006).

55. Lucchi, R. G., & Rebesco, M. Glacial contourites on the Antarctic Peninsula margin: insight for palaeoenvironmental and palaeoclimatic conditions. *Geol. Soc. London Spec. Publ.* **276**(1), 111-127 (2007).

56. Escutia, C., Eittreim, S. L., & Cooper, A. Cenozoic glaciomarine sequences on the Wilkes Land continental rise, Antarctica. *VII International Symposium on Antarctic Earth Sciences Proceedings Volume* 791–795 (1997).

57. Escutia, C., et al. Current controlled deposition on the Wilkes Land continental rise, Antarctica. *Geol. Soc. London Mem.* **22**(1), 373-384 (2002).

58. Donda, F., Brancolini, G., De Santis, L., & Trincardi, F. Seismic facies and sedimentary processes on the continental rise off Wilkes Land (East Antarctica): evidence of bottom current activity. *Deep Sea Res. Part II: Top. Stud. Oceanogr.* **50**(8-9), 1509-1527 (2003).

59. Hesse, R. et al. Asymmetrical turbid surface-plume deposition near ice-outlets of the Pleistocene Laurentide ice sheet in the Labrador Sea. *Geo-Marine Letters* **17**(3), 179-187 (1997).

60. Beaman, R. J., O'Brien, P. E., Post, A. L., & De Santis, L. A New High-Resolution Bathymetry Model for the Terre Adélie and George V Continental Margin, East Antarctica. *Antarctic Science* **23**(1), 95–103 (2011).

61. Cooper, A. K., Barrett, P. J., Hinz, K., Traube, V., Letichenkov, G., & Stagg, H. M. J. Cenozoic prodrading sequences of the Antarctic continental margin: a record of glacio-eustatic and tectonic events. *Marine Geology* **102**, 175-213 (1991).

62. Rebesco, M., & Camerlenghi, A. Late Pliocene margin development and mega debris flow deposits on the Antarctic continental margins, Evidence of the onset of modern Antarctic Ice Sheet? *Palaeogeogr. Palaeoclimat. Palaeoecol.* **260**(1-2), 149–167 (2008).

63. Presti, M., De Santis, L., Busetti, M., & Harris, P. T. Late Pleistocene and Holocene sedimentation on the George V Continental Shelf, East Antarctica. *Deep Sea Res. Part II* **50**(8-9) 1441-1461 (2003).

64. Orsi, A. H., Whitworth, T., & Nowlin, W. D. On the meridional extent and fronts of the Antarctic Circumpolar Current. *Deep Sea Res. Part I* **42**(5), 641-673 (1995).

65. Dowsett, H. J. et al. Assessing confidence in Pliocene sea surface temperatures to evaluate predictive models. *Nature Clim. Change* **2**(5), 365-371 (2012).

66. Whitehead, J. M., & Bohaty, S. M. Pliocene summer sea surface temperature reconstruction using silicoflagellates from Southern Ocean Site 1165. *Paleoceanography* **18**(3), (2003).

67. Hillenbrand, C., and Cortese, G. Polar stratification: A critical view from the Southern Ocean. *Palaeogeogr. Palaeoclimat. Palaeoecol.* **242**(3-4), 240-252 (2006).

68. Denton, G. H., et al. The last glacial termination. *Science* **328**(5986), 1652-1656 (2010).

69. Williams, G. D., & Bindoff, N. L. Wintertime oceanography of the Adélie Depression. *Deep Sea Res. Part II* **50**(8), 1373-1392 (2003).